THE JOURNAL OF PHYSICAL CHEMISTRY C

Article

Cite This: J. Phys. Chem. C 2018, 122, 25035−25042

pubs.acs.org/JPCC

Mechanical Properties Obtained by Indentation of Hollow Pd Nanoparticles

Felipe J. Valencia,[†,‡,▽] Rafael I. González,[§,▽] H. Vega,[∥] Carlos Ruestes,[⊥] José Rogan,[†,▽] Juan Alejandro Valdivia,[†,▽] Eduardo M. Bringa,[§,#] and Miguel Kiwi*[,†,▽]

[†]Departamento de Física, Facultad de Ciencias, Universidad de Chile, Casilla 653, Santiago 7800024, Chile

[‡]Núcleo de Matemáticas, Física y Estadística, Facultad de Ciencias, Universidad Mayor, Santiago 7500628, Chile

[§]Centro de Nanotecnología Aplicada, Facultad de Ciencias, Universidad Mayor, Santiago 8580745, Chile

[∥]Programa de Fisiología y Biofísica, Instituto Ciencias Biomédicas, Facultad de Medicina Universidad de Chile Independencia, Santiago 1027, Chile

[⊥]CONICET and Facultad de Ciencias Exactas y Naturales, Universidad Nacional de Cuyo, Mendoza 5500, Argentina

[#]CONICET and Facultad de Ingeniería, Universidad de Mendoza, Mendoza 5500, Argentina

[▽]Centro para el Desarrollo de la Nanociencia y la Nanotecnologí a, CEDENNA, Avda. Ecuador 3493, Santiago 9170124, Chile

Supporting Information

ABSTRACT: Palladium nanoparticles are technologically important for catalysis, hydrogen storage, and many other applications. Here, we investigate the mechanical properties of Pd hollow nanoparticles of different sizes and thicknesses by means of classical molecular dynamics simulations. Hollow nanospheres of sizes ranging from 5 to 40 nm are compressed using planar indenters. Our results suggest that the mechanical response of hollow nanoparticles can be tailored by tuning the external radius (R) and shell thickness (ω). The largest elastic limit for a given thickness is achieved when the aspect ratio $A = R/\omega$ is $3 \leq A \leq 4$. This delay of the onset of plastic deformation is due to the fact that, for this geometry, hollow nanoparticles can buckle, avoiding stress concentration in the contact; this in turn favors stress accumulation and dislocation emission at the inner surface, in sharp contrast to the behavior of solid nanoparticles and "bulk" surfaces.

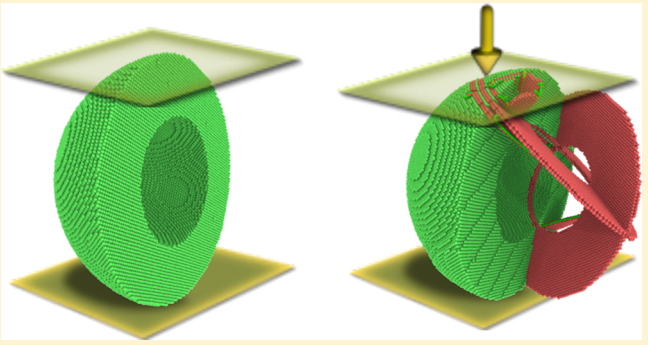

INTRODUCTION

Hollow nanoparticles (hNPs) have attracted much interest, especially for use in nanotechnology. In fact, they have outstanding performance in plasmonics,[1] catalysis,[2] drug delivery,[3] gas storage,[4−6] and other applications. Their main features, low density and high specific surface area, are responsible for the efficiency enhancement relative to conventional solid nanoparticles (NPs). A less explored area is related to their mechanical properties, probably due to the fact that hNPs are perceived as fragile structures, unstable against any perturbation that could trigger hNP failure or collapse[7−10] into a solid NP. However, Shan et al.[11] proved that CdSe hNPs of about 500 nm can be subject to large stress without collapsing. Moreover, it was recently shown that hNPs of sizes no larger than 20 nm can withstand even hypervelocity impacts.[12] In addition, several authors have suggested that hollow interior macroscopic spherical particles could be used as protective coating for space vehicles.[13−15]

Highly porous materials, such as aerogels,[16] nanofoams,[17,18] and bioinspired composites,[19] are also very attractive, since they display a combination of flexibility and toughness. Therefore, based on all these facts, it is natural to think that hNPs can display not only the required strength, but also increased flexibility. Precisely that is the main focus of the present contribution.

Studies of the mechanical properties of NPs are generally carried out by compression using flat indenters.[20] Mechanical properties of a NP can differ significantly from bulk properties, leading for instance to large pseudoelasticity[13,21] and size-dependent strength.[21−24] Experimentally, it has become possible to perform indentation of nanoparticles[25,26] and study the induced defects with in situ high-resolution electron microscopy.[27]

Experimental studies are often supplemented by molecular dynamics (MD) simulations, which can model particles of up to tens of nanometer in diameter, and provide information not

Received: July 28, 2018
Revised: October 2, 2018
Published: October 4, 2018

DOI: 10.1021/acs.jpcc.8b07242
J. Phys. Chem. C 2018, 122, 25035−25042

only on constitutive models for elasticity, but also on plasticity beyond the elastic limit. MD simulations of plasticity are usually carried out for NPs with face-centered cubic (fcc) structure.[28−37]

Despite the above advances for solid NPs, experimental studies of the mechanical properties of hollow NP are still relatively scarce. However, there are studies for CdS,[38] amorphous carbon,[39] silica,[11,40,41] and other elements, all of which indicate that hNPs are able to withstand large stresses. Recently, the anomalous lattice expansion of Ni hNP was studied,[42] for radii of ≈50−100 nm and shell thicknesses of ≈10−25 nm. It may be noted that many studies include the finite element method (FEM) simulations of hollow NP compression, considering only elastic behavior.[38,39,43] However, FEM simulations require constitutive models, which may not be available at the nanoscale. In addition, despite advances on synthesis and experimental techniques, we are not aware of any published simulation on mechanical properties of metallic hNPs.

Several MD simulations[6,7,44−46] tried to elucidate how the stability of hNPs depends on wall thickness and external radius, since it is expected that the mechanical properties of hNPs are mainly determined by these two parameters. Recently, the behavior of Si hNPs was studied using MD simulations.[34] Buckling and amorphization were found for thin shells ($A = R_{ext}/\omega > 5$), whereas dislocation nucleation occurred for thicker shells.

Among all of the diverse hNPs reported in the literature, here we focus our interest on the nanoindentation response of palladium hNPs, since Pd is among the most important materials for catalysis and H storage[47−52] because of its capability to dissociate H_2 under room-temperature conditions. Even more, in 2016, we proposed[6] to use Pd hNPs as hydrogen nanocontainers as a result of MD simulations, something that was achieved experimentally very recently by Shervani et al.[53] This makes the development of Pd-based high strength and elasticity materials an ideal candidate to improve hydrogen technologies.[54] Recently Pd NPs have been shown to behave as efficient carbon scavengers,[55] and since hNPs would be easier to deform and more mobile, they may improve performance.

METHODS

The mechanical properties of hNPs are calculated by molecular dynamics (MD) simulations, as implemented in the LAMMPS code.[56] The interaction between Pd atoms is simulated using the embedded atom method potential,[57] with the parameters by Sheng et al.[58] This potential compares extremely well with density functional theory calculations and experiments, reproducing properties, such as elastic constants,[59] generalized stacking fault (SF) surface energies,[60] bulk modulus, and the equation of state[61] for pressures up to 100 GPa. All of the hNPs were constructed following the standard procedure already employed for other metallic hNPs, such as Au,[7,8,45] Ag,[44] Pt,[62] and Pd.[6,12] The method consists in cutting out two concentric spheres of the Pd lattice, and this way generating nanostructures with an external radius of $5a_0 < R_{out} < 45a_0$ (or 1.95 nm $< R_{out} <$ 17.91 nm) and thicknesses of $5a_0 < \omega < 10a_0$ (or 1.95 nm $< R_{out} <$ 3.89 nm), where a_0 = 0.389 nm corresponds to the Pd lattice parameter. Experimentally hNPs of these sizes have been synthesized using galvanic replacement.[50,51]

Cutting the crystal lattice is likely to create hNPs far from equilibrium and subject to some remnant stress due to the cavity presence. For the hNP atoms to reach a minimum energy configuration, a conjugate gradient minimization, followed by a FIRE minimization,[63] and ending with a MD relaxation of 0.5 ns at 300 K, was carried out.

Indentation was performed using a flat indenter to mimic experimental conditions.[21] To describe the interaction of the indenter surface and the hNP, we adopted a potential of the form[64]

$$U(z) = K(z - z_0)^3 \tag{1}$$

where z_0 is the indenter position and K = 10 eV/Å^3 is the constant, which describes the indenter stiffness. Before the indentation is performed, the relaxed hNP is located on a fixed flat surface subject to the potential of eq 1; next the structure is relaxed to adapt the contact area of the hNP.

We adopted this procedure to check for possible defect nucleation due to contact with the NP substrate. Jiang et al.[44] modeled the deformation of hNPs during sintering focusing on the neck dynamics of two different-sized hNPs. They found that these two hNPs can nucleate SFs when in contact, a behavior not observed for solid NPs, where the presence of a substrate or the sintering between them did not nucleate a significant defect concentration, other than surface reconstruction or rotations. In our simulations, defects were not observed after relaxation of the hNP on the substrate.

Previous authors have established that MD indentation compression rates of 10^8 s^{-1} (1.0 m/s) are typically sufficient to capture the physics of the problem both for bulk and NPs.[65] However, our simulations suggest a more stringent requirement of 10^7 s^{-1} (0.1 m/s) for hNPs. This criterion was adopted since the largest aspect ratio hNPs we study are prone to collapse, even at room temperature. This insures that the largest aspect ratio hNPs in contact with the indenter do not collapse, and large fluctuations of the stress−strain plot, related to the hNP breathing modes, are avoided.

All indentation tests were carried out at 300 K, and the system temperature was controlled by means of a velocity rescaling algorithm, with a timestep of 1.0 fs. Finally, all of the hNPs were compressed up to 15%. On the other hand, after the desired strain is achieved, the flat indenter is kept fixed during 0.2 ns before the unload process is started.

Defect analysis was carried out using common neighbor analysis (CNA) and the polyhedral template matching method,[66] both implemented in OVITO.[67] Dislocations were identified with the DXA algorithm, and defective atoms, such as stacking faults (SF) or twin boundaries, were analyzed with the Crystallographic Analysis Tool code.[68]

The stress−strain relations are obtained on the basis of the contact area and the indenter force. To determine the indenter contact area, we compute the number of atoms in the indenter neighborhood, on the basis of the rule that $|z - z_0| < 0.2$ Å (where z and z_0 are the vertical positions of the atom and the surface, respectively) following the method proposed by Ziegenhain et al.[69] The elastic behavior of Pd is described completely by the elastic constants C_{11}, C_{12}, and C_{44}. The values of the Pd elastic constants by Sheng et al.[58] were used to calculate the orientation-dependent elastic modulus for (100) single crystals by means of the following equation[70]

$$\frac{1}{E_{100}} = \frac{C_{11} + C_{12}}{(C_{11} + 2C_{12})(C_{11} - C_{12})} \tag{2}$$

DOI: 10.1021/acs.jpcc.8b07242
J. Phys. Chem. C 2018, 122, 25035−25042

which renders E_{100} = 79 GPa.

RESULTS

The stress−strain plots of Figure 1 (and Figure S1 of the Supporting Information) show that the Pd hNP mechanical

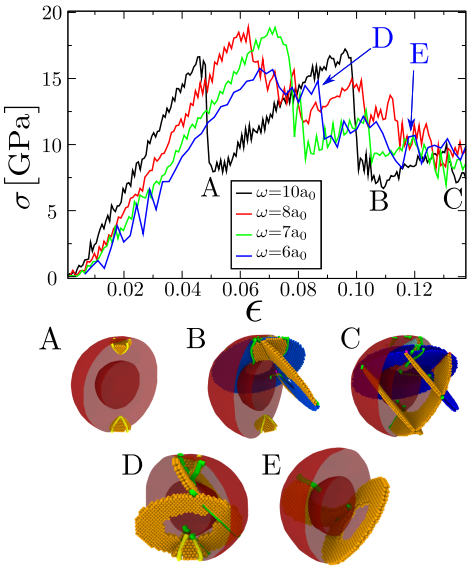

Figure 1. Deformation under loading of hNPs with an aspect ratio of 2 and different thicknesses. (A), (B), and (C) show dislocation formation for the $\omega = 10a_0$ hNP, whereas (D) and (E) display dislocations for a hNP of thickness $\omega = 6a_0$. Orange and blue colors represent Pd atoms belonging to SFs and twin boundaries, respectively. Different coordination atoms are removed from the figure. The red region delimits the hNP inner and outer surfaces. The green and yellow lines represent Shockley and Hirt dislocations, respectively.

behavior is strongly dependent on the thickness ω and the aspect ratio ($A = R_{out}/w$). A linear regime is observed, which reaches all of the way up to between 5% and almost 8% strain, for $\omega = 10a_0$ and $6a_0$, respectively, beyond these strain values dislocation plasticity sets in. However, several differences are observed in the plastic regime: for $\omega = 10a_0$, $8a_0$, and $7a_0$, a second linear region, after the first partial drop, is observed; it corresponds to the formation of a SF tetrahedron in the contact region, as shown in Figure 1A. This structure was already observed for Al NP by Salah et al.,[32] who showed that the edges of the surface in contact with the indenter concentrate a large stress, leading to the nucleation of four {111} partial dislocations.

hNPs display a second yield stress in association to the gliding SF planes of the tetrahedron, which leads to twin formation not observed in Al NP,[32] as shown in Figure 1B. On the other hand, in the thinner shell case ($\omega = 6a_0$), the first partial dislocation emitted is rapidly absorbed by the inner surface, before a second Shockley partial dislocation can interact with it; thus, the formation of a perfect SF tetrahedron on the upper indenter with junctions, which can act as further dislocation sources, is not feasible (Figure 1D). From the simulations, the critical thickness to observe the SF tetrahedron is $\omega = 7a_0$. Below this thickness, the pyramidal structure can disappear quasielastically, as seen in Figure 1E.

The elastic response of hollow spheres can be treated by means of different theories depending on the ratio of the thickness w to midradius R_{mid}, namely, $Z = \omega/R_{mid}$. For $Z \leq 1/10$, the classical thin shell theory is the best choice due to the simplicity of its solution and sufficient accuracy; under this theory, transverse shear deformation is neglected. For $Z > 1/10$, however, an accurate representation of the "true" values of the stress distribution of a hollow sphere compressed by equal and opposite axial loads can be determined by allowing transverse shear deformation in the formulation. In general, the calculation of the elastic moduli of thin-shelled spheres is analyzed using the theory by Reissner,[71,72] and although it was not originally developed for cases in which $Z > 1/10$, its accuracy was tested by Gregory et al.,[73] rendering values closer to the true ones than those of classical thin shell theory, due to the inclusion of transverse shear deformation. Under Reissner's theory, for a given indentation δ (less than the shell thickness w), the force F on a spherical shell of radius R, elastic modulus E, and Poisson's ratio ν, are given by

$$F = \frac{4E_{100}w^2\delta}{R\sqrt{3(1-\nu^2)}} \quad (3)$$

The predictions of this last equation are illustrated in Figure 2, with remarkable agreement to the simulations for two

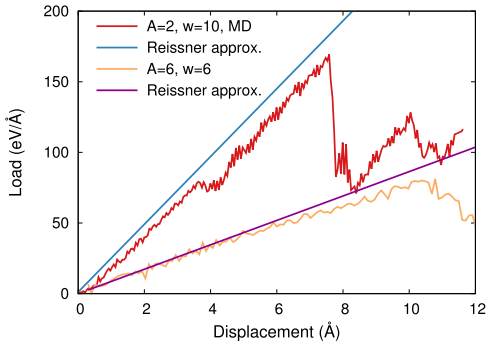

Figure 2. Comparison of two loading plots using the elastic approximation derived from Reissner's theory.

distinctive cases. This finding not only supports the statement by Gregory et al.[73] of the applicability of the theory to a different aspect ratio by considering the transverse shear deformation but also shows that the model is likely to hold for nanoscale systems like the ones studied here.

In Figure 3, the compression of a hNP defined by $\omega = 5a_0$ and $A = 4$ is illustrated. For this particular combination of geometrical parameters, the first dislocation emission occurs from the inner surface, contrary to what is observed for solid NP indentation. It is important to note that simulations for Si hNPs showed dislocation nucleation from the inner surface,[34] for a certain range of aspect ratios, but this nucleation occurred in the polar region, and not in the equatorial region, as observed here. Before the first dislocation appears, the CNA algorithm detects an unusually large concentration of body-centered cubic (bcc) atoms in the equatorial region (Figure 3g); however, further analysis using the PMT method shows that the bcc atoms are fcc atoms in regions with large strain concentration. The large strain and stress observed in the inner surface act as the seed for the partial dislocation nucleation, as shown in Figure 3a−c. After dislocations propagate and new SFs are nucleated, a twin boundary also originates from the inner surface, as shown in Figure 3d. Even after the loss of symmetry due to the first dislocation, the subsequent

DOI: 10.1021/acs.jpcc.8b07242
J. Phys. Chem. C 2018, 122, 25035−25042

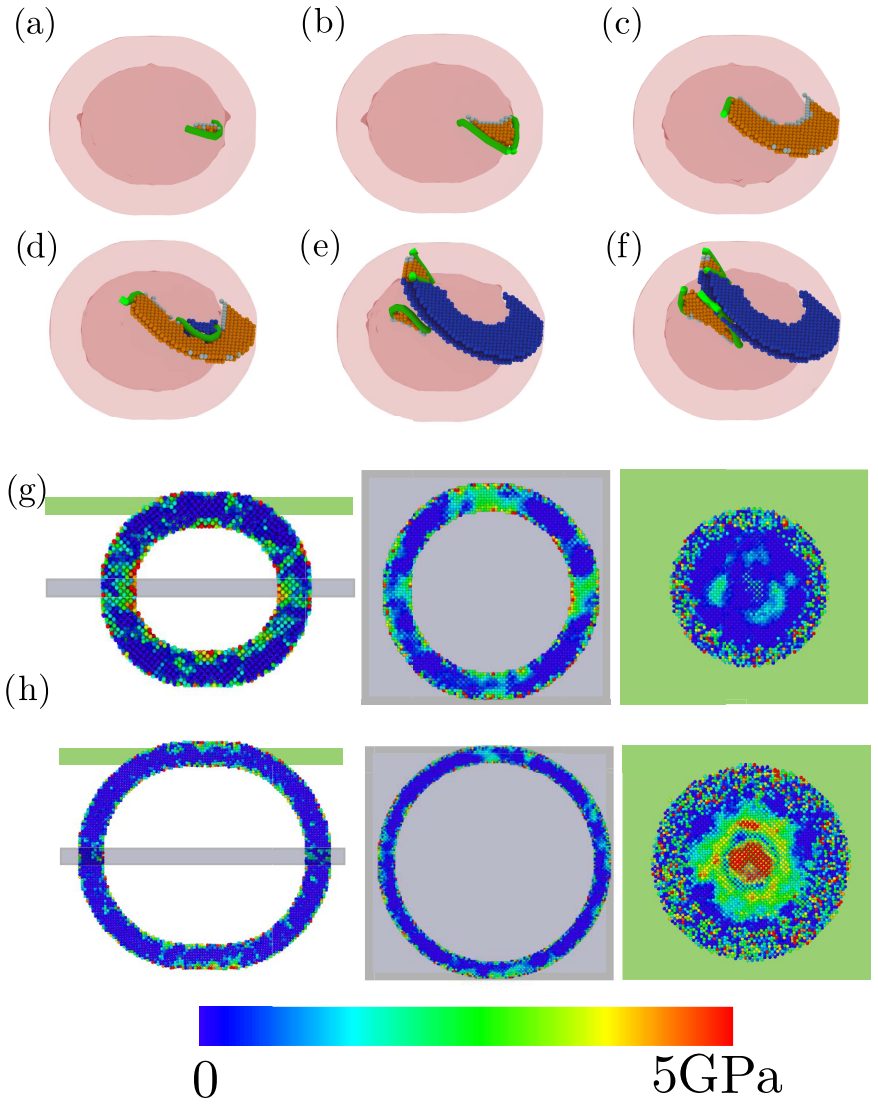

Figure 3. (a–f) Nucleation of dislocations during the indentation of a hNP of $\omega = 5a_0$ and $A = 4$ at different strains. The orange and blue atoms correspond to SFs and twin boundaries, respectively; the green lines are Shockley partial dislocations. (g, h) The stress distribution for a planar cut at $\epsilon = 6\%$, for hNPs of aspect ratio $A = 4$ and 7, respectively. The gray cuts illustrate the stress in the equatorial region, and the green ones in polar region.

dislocations also originate in the equatorial region (see Figure 3f), on the basis of the same mechanism than the first one. The fact that a second dislocation emitted from the inner surface does take place implies that this mechanism is not restricted only to the highly symmetric case. It is important to keep in mind that hNPs with uniform thicknesses and sizes, and without surface irregularities or defects, are difficult to obtain experimentally.

In Figure 3h, the shear strain distribution is illustrated for a hNP with $\omega = 4a_0$ and $A = 7$. Contrary to the $A = 4$ case, the strain in the equatorial region is almost uniform. However, the stress concentration appears close to the indenter region; therefore, it is expected that dislocations will be generated close to the contact surface.

A solid NP reaches an elastic limit of around 3% for $R = 10$ nm, whereas a hNP with $\omega = 2.5$ nm reaches nearly a 7% elastic limit. This much larger elastic limit is a general feature for hNPs. To construct Figure 4, several stress–strain plots were calculated for different values of ω and A, and they were classified according to the two-dimensional phase diagram proposed by Jiang et al.[7] In Figure 4, it is observed that the hNP elastic limit and strength decrease for extreme values of A or ω. However, two quite different scenarios emerge. If ω remains constant and A is large enough, the hNP becomes thermally unstable due to the presence of the cavity, and the spherical shape cannot be maintained under ambient conditions. On the other hand, for large ω values, the hNP tends to behave as a compact NP. From the diagram we obtain that the maximum elastic deformation and stress that a hNP can achieve is ≈11% and ≈20 GPa, respectively. This limit is reached in the neighborhood of $3 \leq A \leq 4$ and is larger than for other Pd nanostructures.[54,74] It is worth noticing that the improvement of the mechanical properties, for these specific A values, matches with the fact that the dislocations are nucleated from the hNP inner surface and not from the indenter contact region.

Si hNPs with $R = 20$ nm and shell thickness $\omega = 2–15$ nm display a maximum critical strain (before plasticity) close to $\omega/R = 0.2$ and a maximum critical stress close to $\omega/R = 0.5$. In this study, we observe a rich behavior, which also depends on

DOI: 10.1021/acs.jpcc.8b07242
J. Phys. Chem. C 2018, 122, 25035–25042

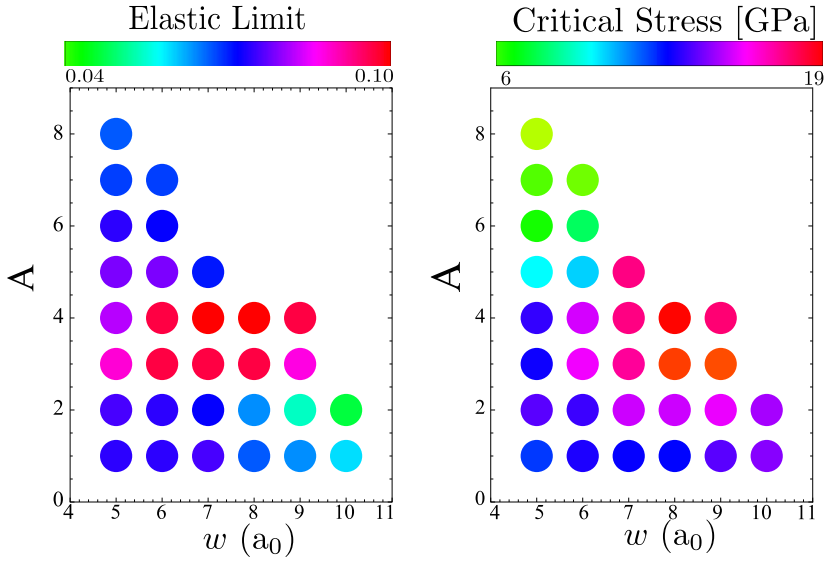

Figure 4. Elastic limit (left) and critical stress (right) as function of thickness ω and aspect ratio A. $A = 1$ corresponds to a nonhollow spherical NP.

A. These results are in contrast to the monotonic behavior of the often observed critical NP stress, as for example in the work of Mordehai et al.,[22] Millán et al.,[30] and in this work for $A = 1$ values (solid NP). Buckling models, which work well at the micron scale,[39] do not seem to be predictive at the nanoscale. Buckling was observed[34] for Si hNPs for values of $\omega/R < 0.2$, however, only slight buckling was observed in our simulations, but it is expected for somewhat larger Pd hNPs (for $\omega/R < 0.1$), but it is quite unlikely that Pd hNPs will be able to withstand the cavity-induced stress without collapsing.

hNP load vs strain plots along the {111} and {100} orientations are compared in Figure 5. Both structures have the same external radii and thicknesses. As expected, orientation changes the slope in the elastic regime, the elastic limit, and also the plasticity. For the {111} orientation, dislocations appear for a 5% strain, whereas in the {100} orientation, they appear for an 8% strain. The main difference is that the {100} orientation leads to the formation of a large SF over the entire NP, followed by a twin associated to a second linear regime. As expected from the available {111} planes, in contrast to the four {100} planes, case, {111} compression leads to the formation of three SFs in the contact region, activated by the same mechanism that generated the SF tetrahedron.[32] However, in this case, the Shockley partial dislocations interact forming a stair-rod (Figure 5C) dislocation according to

$$\frac{1}{6}[\bar{1}2\bar{1}] + \frac{1}{6}[1\bar{1}2] \rightarrow \frac{1}{6}[011]$$

In Figure 5D, it is observed that larger strain leads to the formation of additional partial dislocations. These SFs are also nucleated from the surface contact edges and therefore follow the orientation of the SF, nucleated previously. At 15% strain, all emitted partial dislocations remain confined to the polar region in between the SF pyramids, a result which is different from the {100} case, where SFs or twin planes are expected over the whole hNP for such large deformations. Interestingly enough, the compression for these two cases gives a somewhat similar response in the elastic regime, with {111} being slightly stiffer, as expected from the magnitudes of the corresponding elastic moduli.

Finally, different load−unload plots for 7.5, 8.0, 11.0, and 15.0% were obtained, as illustrated in Figure 6. After compressions of 8.0, 11.0, and 15.0%, the hNPs are permanently modified after removing the indenter, whereas for 7.5%, a full recovery of the initial shape results consistent to a reversible elastic response. It is worth noticing that for 7.5%, all of the defective atoms belong to the SF tetrahedron that forms in the indenter contact region, disappear once the indenter is removed. For larger strains, permanent modifications are associated to twin formation, which induce size and shape changes and the appearance of surface steps.

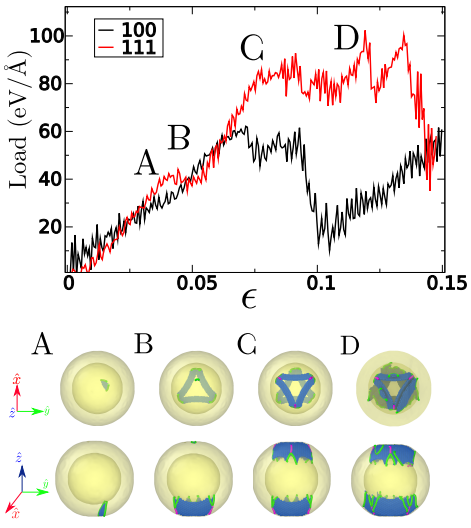

Figure 5. Indenter force as a function of strain for a {111} and a {100} hNP. Both nanostructures are $\omega = 2.5$ nm wide and $R = 15$ nm in diameter. The yellow region delimits the inner and outer surfaces. (A), (B), (C), and (D) correspond to different stages of the {111} hNP indentation process. The top figures show dislocations and defects observed from the indenter perspective ($\hat{z}$), whereas the bottom panels show an outside view, both cases represent the same {111} indentation. In the figure, the green and pink lines correspond to Shockley and stair-rod dislocations and the blue regions denote atoms that belong to stacking faults.

DOI: 10.1021/acs.jpcc.8b07242
J. Phys. Chem. C 2018, 122, 25035−25042

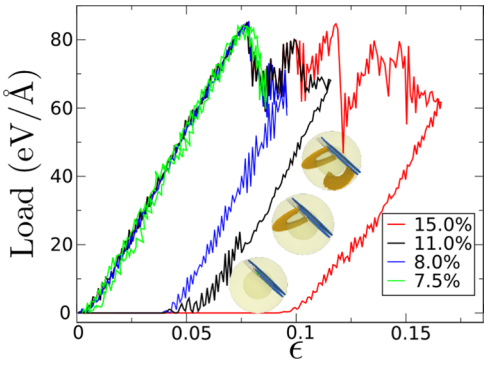

Figure 6. Load−unload plots for different deformations. The hNP has a radius of $18a_0$ and a thickness of $9a_0$. The yellow atoms correspond to SFs, the blue atoms to a twin boundary, and the white atoms represent an intrinsic SF.

DISCUSSION AND CONCLUSIONS

Elastic−plastic transitions of palladium hollow nanoparticles can be tuned by control of their thicknesses and radii. Large hNPs can withstand severe strain before plastic deformation sets in. The largest strains measured are associated to some surface bucklings, which allow a stress accumulation in the internal surface, either in the equatorial or polar region and act as an impediment for atoms below the indenter to form partial dislocations. This mechanism can lead to nucleation originating from the equatorial inner surface, contrary to the assertion that atoms below the indenter control the initiation of plastic deformation.[32,75] This result may have interesting applications in industry.

The best performance of hNPs is obtained when the aspect ratio is close to $A = 4$, reaching nearly 10% strain and supporting an almost 20 GPa stress, better than other Pd nanostructures. For a larger aspect ratio, the hNP elastic limit and strength decrease due to the fact that the stress induced by the cavity dominates dislocation nucleation, and thermal stability[6,7,46] can lead the partial collapse of the hNP.

Orientation plays a major role in the deformation mechanism, as expected. In contrast to the {100} case, plasticity for the {111} orientation starts much earlier, at 5%, however, dislocations are confined to the polar region and adopt a triangular pyramid structure, product of stair-rod dislocations, which remain stable even at 15% strain. Stair-rod junctions require a large stress to act as dislocation sources, acting as a barrier for partial dislocations nucleated from the polar region.

Although we studied Pd hNPs due to their importance for hydrogen-based technologies[54] a similar behavior is to be expected for other fcc metals. It would be interesting to explore metals with different twinnabilities, which might lead to variations in hardening after plastic yielding.[76]

Arrays of hNPs could also display excellent mechanical properties with reduced weight, as was recently shown for silica[77] hNPs. Metallic hNP arrays might be able to achieve remarkably large elastic limits before NP densification and sintering occur. In addition to hNPs, other highly porous nano-objects, such as nanotubes,[78] nanoframes,[79] nanocubes,[80,81] and/or elastic membranes,[32,82] could also manifest unexpected mechanical properties.

ASSOCIATED CONTENT

Supporting Information

The Supporting Information is available free of charge on the ACS Publications website at DOI: 10.1021/acs.jpcc.8b07242.

Stress−strain plots (Figure S1); values of ω, A, ε, and σ (Table S1) (PDF)

AUTHOR INFORMATION

Corresponding Author

*E-mail: m.kiwi.t@gmail.com.

ORCID

Rafael I. González: 0000-0003-2599-8404

Miguel Kiwi: 0000-0001-8580-1912

Notes

The authors declare no competing financial interest.

ACKNOWLEDGMENTS

This work was supported by the Fondo Nacional de Investigaciones Cientificas y Tecnológicas (FONDECYT, Chile) under grants #1160639 (M.K. and J.R.), AFOSR Grant FA9550-16-1-0122, and Financiamiento Basal para Centros Cientificos y Tecnológicos de Excelencia FB-0807 (R.I.G., F.J.V., M.K., J.R., and J.A.V.). E.M.B. thanks support from PICT-2014-0696 (ANPCyT) and M003 (SeCTyP-UN Cuyo) grant. C.R. thanks support from PICT-2015-0342 (ANPCyT). F.J.V. was supported by CONICYT Doctoral Fellowship grant #21140948. This research was partially supported by the supercomputing infrastructure of the NLHPC (ECM-02).

REFERENCES

(1) Liang, H.-P.; Wan, L.-J.; Bai, C.-L.; Jiang, L. Gold Hollow Nanospheres: Tunable Surface Plasmon Resonance Controlled by Interior-Cavity Sizes. *J. Phys. Chem. B* **2005**, *109*, 7795−7800.

(2) Chen, H. M.; Liu, R.-S.; Lo, M.-Y.; Chang, S.-C.; Tsai, L.-D.; Peng, Y.-M.; Lee, J.-F. Hollow Platinum Spheres with Nano-Channels: Synthesis and Enhanced Catalysis for Oxygen Reduction. *J. Phys. Chem. C* **2008**, *112*, 7522−7526.

(3) Li, Z.-Z.; Wen, L.-X.; Shao, L.; Chen, J.-F. Fabrication of Porous Hollow Silica Nanoparticles and Their Applications in Drug Release Control. *J. Controlled Release* **2004**, *98*, 245−254.

(4) Lou, X. W.; Wang, Y.; Yuan, C.; Lee, J. Y.; Archer, L. A. Template-Free Synthesis of SnO_2 Hollow Nanostructures with High Lithium Storage Capacity. *Adv. Mater.* **2006**, *18*, 2325−2329.

(5) Xie, L.; Zheng, J.; Liu, Y.; Li, Y.; Li, X. Synthesis of Li_2NH Hollow Nanospheres with Superior Hydrogen Storage Kinetics by Plasma Metal Reaction. *Chem. Mater.* **2008**, *20*, 282−286.

(6) Valencia, F. J.; González, R. I.; Tramontina, D.; Rogan, J.; Valdivia, J. A.; Kiwi, M.; Bringa, E. M. Hydrogen Storage in Palladium Hollow Nanoparticles. *J. Phys. Chem. C* **2016**, 23836.

(7) Jiang, L.; Yin, X.; Zhao, J.; Liu, H.; Liu, Y.; Wang, F.; Zhu, J.; Boey, F.; Zhang, H. Theoretical Investigation on the Thermal Stability of Hollow Gold Nanoparticles. *J. Phys. Chem. C* **2009**, *113*, 20193−20197.

(8) Jiang, L.; Sun, W.; Gao, Y.; Zhao, J. Geometric Thermal Phase Diagrams for Studying the Thermal Dynamic Stability of Hollow Gold Nanoballs at Different Temperatures. *Phys. Chem. Chem. Phys.* **2014**, *16*, 6623−6629.

(9) Nakamura, R.; Tokozakura, D.; Lee, J.-G.; Mori, H.; Nakajima, H. Shrinking of Hollow Cu_2O and NiO Nanoparticles at High Temperatures. *Acta Mater.* **2008**, *56*, 5276−5284.

(10) Glodán, G.; Cserháti, C.; Beke, D. L. Temperature-Dependent Formation and Shrinkage of Hollow Shells in Hemispherical Ag/Pd Nanoparticles. *Philos. Mag.* **2012**, *92*, 3806−3812.

DOI: 10.1021/acs.jpcc.8b07242
J. Phys. Chem. C 2018, 122, 25035−25042

(11) Shan, Z. W.; Adesso, G.; Cabot, A.; Sherburne, M.; Asif, S. S.; Warren, O.; Chrzan, D.; Minor, A.; Alivisatos, A. Ultrahigh Stress and Strain in Hierarchically Structured Hollow Nanoparticles. *Nat. Mater.* **2008**, *7*, 947−952.
(12) Valencia, F. J.; González, R. I.; Valdivia, J. A.; Kiwi, M.; Bringa, E. M.; Rogan, J. Inducing Porosity on Hollow Nanoparticles by Hypervelocity Impacts. *J. Phys. Chem. C* **2017**, *121*, 17856−17861.
(13) Zeng, H.; Pattofatto, S.; Zhao, H.; Girard, Y.; Fascio, V. Perforation of Sandwich Plates with Graded Hollow Sphere Cores Under Impact Loading. *Int. J. Impact Eng.* **2010**, *37*, 1083−1091.
(14) Cour-Palais, B. G. In *Space Vehicle Meteoroid Shielding Design*, Comet Halley Micrometeoroid Hazard Workshop, 1979.
(15) Li, Y.; Li, J. B.; Zhang, R. Energy-Absorption Performance of Porous Materials in Sandwich Composites Under Hypervelocity Impact Loading. *Compos. Struct.* **2004**, *64*, 71−78.
(16) Parmenter, K. E.; Milstein, F. Mechanical Properties of Silica Aerogels. *J. Non-Cryst. Solids* **1998**, *223*, 179−189.
(17) Ruestes, C. J.; Schwen, D.; Millán, E. N.; Aparicio, E.; Bringa, E. M. Mechanical Properties of Au Foams Under Nanoindentation. *Comput. Mater. Sci.* **2018**, *147*, 154−167.
(18) Jin, H.-J.; Weissmüller, J.; Farkas, D. Mechanical Response of Nanoporous Metals: A Story of Size, Surface Stress, and Severed Struts. *MRS Bull.* **2018**, *43*, 35−42.
(19) Wegst, U. G.; Bai, H.; Saiz, E.; Tomsia, A. P.; Ritchie, R. O. Bioinspired Structural Materials. *Nat. Mater.* **2015**, *14*, 23.
(20) Palacio, M. L.; Bhushan, B. Depth-Sensing Indentation of Nanomaterials and Nanostructures. *Mater. Charact.* **2013**, *78*, 1−20.
(21) Sun, J.; He, L.; Lo, Y.-C.; Xu, T.; Bi, H.; Sun, L.; Zhang, Z.; Mao, S. X.; Li, J. Liquid-Like Pseudoelasticity of Sub-10-nm Crystalline Silver Particles. *Nat. Mater.* **2014**, *13*, 1007.
(22) Mordehai, D.; Lee, S.-W.; Backes, B.; Srolovitz, D. J.; Nix, W. D.; Rabkin, E. Size Effect in Compression of Single-Crystal Gold Microparticles. *Acta Mater.* **2011**, *59*, 5202−5215.
(23) Nowak, J.; Beaber, A.; Ugurlu, O.; Girshick, S.; Gerberich, W. Small Size Strength Dependence on Dislocation Nucleation. *Scr. Mater.* **2010**, *62*, 819−822.
(24) Han, W.-Z.; Huang, L.; Ogata, S.; Kimizuka, H.; Yang, Z.-C.; Weinberger, C.; Li, Q.-J.; Liu, B.-Y.; Zhang, X.-X.; Li, J.; et al. From "Smaller is Stronger" to "Size-Independent Strength Plateau": Towards Measuring the Ideal Strength of Iron. *Adv. Mater.* **2015**, *27*, 3385−3390.
(25) Espinosa, H. D.; Bernal, R. A.; Filleter, T. In situ TEM Electromechanical Testing of Nanowires and Nanotubes. *Small* **2012**, *8*, 3233−3252.
(26) Chen, C.-C.; Zhu, C.; White, E. R.; Chiu, C.-Y.; Scott, M.; Regan, B.; Marks, L. D.; Huang, Y.; Miao, J. Three-Dimensional Imaging of Dislocations in a Nanoparticle at Atomic Resolution. *Nature* **2013**, *496*, 74.
(27) Carlton, C. E.; Ferreira, P. In Situ TEM Nanoindentation of Nanoparticles. *Micron* **2012**, *43*, 1134−1139.
(28) Bian, J.-J.; Wang, G.-F. Atomistic Deformation Mechanisms in Copper Nanoparticles. *J. Comput. Theor. Nanosci.* **2013**, *10*, 2299−2303.
(29) Wang, G.; Bian, J.; Feng, J.; Feng, X. Compressive Behavior of Crystalline Nanoparticles with Atomic-Scale Surface Steps. *Mater. Res. Express* **2015**, *2*, No. 015006.
(30) Millán, E. N.; Tramontina, D. R.; Urbassek, H. M.; Bringa, E. M. The Elastic-Plastic Transition in Nanoparticle Collisions. *Phys. Chem. Chem. Phys.* **2016**, *18*, 3423−3429.
(31) Zheng, B.; Wang, Y.-N.; Qi, M.; Du, H. Extended Dislocations in Plastically Deformed Metallic Nanoparticles. *Nanomater. Nanotechnol.* **2016**, *6*, 34.
(32) Salah, S. B. H.; Gerard, C.; Pizzagalli, L. Influence of Surface Atomic Structure on the Mechanical Response of Aluminum Nanospheres Under Compression. *Comput. Mater. Sci.* **2017**, *129*, 273−278.
(33) Yang, L.; Bian, J.-J.; Wang, G.-F. Impact of Atomic-Scale Surface Morphology on the Size-Dependent Yield Stress of Gold Nanoparticles. *J. Phys. D: Appl. Phys.* **2017**, *50*, No. 245302.
(34) Yang, L.; Bian, J.; Zhang, H.; Niu, X.; Wang, G. Size-Dependent Deformation Mechanisms in Hollow Silicon Nanoparticles. *AIP Adv.* **2015**, *5*, No. 077162.
(35) Yu, Q.; Qi, L.; Mishra, R. K.; Zeng, X.; Minor, A. M. Size-Dependent Mechanical Properties of Mg Nanoparticles Used for Hydrogen Storage. *Appl. Phys. Lett.* **2015**, *106*, No. 261903.
(36) Bian, J. J.; Yang, L.; Niu, X.; Wang, G. Orientation-Dependent Deformation Mechanisms of bcc Niobium Nanoparticles. *Philos. Mag.* **2018**, 1848−1864.
(37) Hong, Y.; Zhang, N.; Zaeem, M. A. Metastable Phase Transformation and Deformation Twinning Induced Hardening-Stiffening Mechanism in Compression of Silicon Nanoparticles. *Acta Mater.* **2018**, *145*, 8−18.
(38) Zhang, L.; D'Acunzi, M.; Kappl, M.; Auernhammer, G. K.; Vollmer, D.; van Kats, C. M.; van Blaaderen, A. Hollow Silica Spheres: Synthesis and Mechanical Properties. *Langmuir* **2009**, *25*, 2711−2717.
(39) Yang, W.; Yang, J.; Dong, Y.; Mao, S.; Gao, Z.; Yue, Z.; Dillon, S. J.; Xu, H.; Xu, B. Probing Buckling and Post-Buckling Deformation of Hollow Amorphous Carbon Nanospheres: In-Situ Experiment and Theoretical Analysis. *Carbon* **2018**, *137*, 411−418.
(40) Berry, J. D.; Mettu, S.; Dagastine, R. R. Precise Measurements of Capsule Mechanical Properties using Indentation. *Soft Matter* **2017**, *13*, 1943−1947.
(41) Lasio, J.; Allgeier, A. M.; Chan, C. D.; Londono, J. D.; Najafi, E.; Woerner, F. J. Control of Mechanical Stability of Hollow Silica Particles, and Its Measurement by Mercury Intrusion Porosimetry. *Langmuir* **2017**, *33*, 4666−4674.
(42) Iyer, G.; Shervani, S.; Mishra, G.; De, D.; Kumar, A.; Sivakumar, S.; Balani, K.; Pala, R.; Subramaniam, A. Poisson Effect Driven Anomalous Lattice Expansion in Metal Nanoshells. *Appl. Phys. Lett.* **2017**, *110*, No. 131603.
(43) Yin, J.; Retsch, M.; Lee, J.-H.; Thomas, E. L.; Boyce, M. C. Mechanics of Nanoindentation on a Monolayer of Colloidal Hollow Nanoparticles. *Langmuir* **2011**, *27*, 10492−10500.
(44) Jiang, S.; Zhang, Y.; Gan, Y.; Chen, Z.; Peng, H. Molecular Dynamics Study of Neck Growth in Laser Sintering of Hollow Silver Nanoparticles with Different Heating Rates. *J. Phys. D: Appl. Phys.* **2013**, *46*, No. 335302.
(45) Dalgic, S. S. Size Dependent Properties of Hollow Gold Nanoparticles: A Theoretical Investigation. *Acta Phys. Pol., A* **2016**, *129*, 531−534.
(46) Reyes, P. N.; Valencia, F.; Vega, H.; Ruestes, C.; Rogan, J.; Valdivia, J. A.; Kiwi, M. On the Stability of Hollow Nanoparticles and the Simulation Temperature Ramp. *Inorg. Chem. Front.* **2018**, 1139.
(47) Kim, S.-W.; Kim, M.; Lee, W. Y.; Hyeon, T. Fabrication of Hollow Palladium Spheres and Their Successful Application to the Recyclable Heterogeneous Catalyst for Suzuki Coupling Reactions. *J. Am. Chem. Soc.* **2002**, *124*, 7642−7643.
(48) Ge, J.; Xing, W.; Xue, X.; Liu, C.; Lu, T.; Liao, J. Controllable Synthesis of Pd Nanocatalysts for Direct Formic Acid Fuel Cell (DFAFC) Application: From Pd Hollow Nanospheres to Pd Nanoparticles. *J. Phys. Chem. C* **2007**, *111*, 17305−17310.
(49) Liu, Z.; Zhao, B.; Guo, C.; Sun, Y.; Shi, Y.; Yang, H.; Li, Z. Carbon Nanotube/Raspberry Hollow Pd Nanosphere Hybrids for Methanol, Ethanol, and Formic Acid Electro-Oxidation in Alkaline Media. *J. Colloid Interfaces Sci.* **2010**, *351*, 233−238.
(50) Wang, B.; Yang, J.; Wang, L.; Wang, R.; Tian, C.; Jiang, B.; Tian, M.; Fu, H. Hollow Palladium Nanospheres with Porous Shells Supported on Graphene as Enhanced Electrocatalysts for Formic Acid Oxidation. *Phys. Chem. Chem. Phys.* **2013**, *15*, 19353−19359.
(51) Chen, D.; Cui, P.; He, H.; Liu, H.; Yang, J. Highly Catalytic Hollow Palladium Nanoparticles Derived From Silver@Silver-Palladium Core-Shell Nanostructures for the Oxidation of Formic Acid. *J. Power Sources* **2014**, *272*, 152−159.
(52) Tang, S.; Vongehr, S.; Wang, X.; Wang, Y.; Meng, X. Bubble-Assisted Growth of Hollow Palladium Nanospheres with Structure Control Allowing Very Thin Shells for Highly Enhanced Catalysis. *RSC Adv.* **2014**, *4*, 13729−13732.

DOI: 10.1021/acs.jpcc.8b07242
J. Phys. Chem. C 2018, 122, 25035−25042

(53) Shervani, S.; Mukherjee, P.; Gupta, A.; Mishra, G.; Illath, K.; Ajithkumar, T.; Sivakumar, S.; Sen, P.; Balani, K.; Subramaniam, A. Multi-Mode Hydrogen Storage in Nanocontainers. *Int. J. Hydrogen Energy* **2017**, *42*, 24256−24262.
(54) Idrissi, H.; Wang, B.; Colla, M. S.; Raskin, J. P.; Schryvers, D.; Pardoen, T. Ultrahigh Strain Hardening in Thin Palladium Films with Nanoscale Twins. *Adv. Mater.* **2011**, *23*, 2119−2122.
(55) Lu, P.-H.; Xie, D.-G.; Liu, B.-Y.; Ai, F.; Zhang, Z.-R.; Jin, M.-S.; Zhang, X. F.; Ma, E.; Li, J.; Shan, Z.-W. Highly Deformable and Mobile Palladium Nanocrystals as Efficient Carbon Scavengers, arXiv:1802.00207. arXiv.org e-Print archive. https://arxiv.org/abs/1802.00207 (submitted Feb 1, 2018).
(56) Plimpton, S. Fast Parallel Algorithms for Short-Range Molecular Dynamics. *J. Comput. Phys.* **1995**, *117*, 1−19.
(57) Daw, M. S.; Baskes, M. I. Embedded-Atom Method: Derivation and Application to Impurities, Surfaces, and Other Defects in Metals. *Phys. Rev. B* **1984**, *29*, 6443.
(58) Sheng, H.; Kramer, M.; Cadien, A.; Fujita, T.; Chen, M. Highly Optimized Embedded-Atom-Method Potentials for Fourteen fcc Metals. *Phys. Rev. B* **2011**, *83*, No. 134118.
(59) Simmons, G.; Wang, H. *Single Crystal Elastic Constants and Calculated Aggregate Properties*; MIT Press: Cambridge, MA, 1971.
(60) Tyson, W.; Miller, W. Surface Free Energies of Solid Metals: Estimation From Liquid Surface Tension Measurements. *Surf. Sci.* **1977**, *62*, 267−276.
(61) Mao, H. K.; Bell, P.; Shaner, J. W.; Steinberg, D. Specific Volume Measurements of Cu, Mo, Pd, and Ag and Calibration of the Ruby R1 Fluorescence Pressure Gauge From 0.06 to 1 Mbar. *J. Appl. Phys.* **2008**, *49*, 3276−3283.
(62) Shan, A.; Chen, Z.; Li, B.; Chen, C.; Wang, R. Monodispersed, Ultrathin NiPt Hollow Nanospheres with Tunable Diameter and Composition Via a Green Chemical Synthesis. *J. Mater. Chem. A* **2015**, *3*, 1031−1036.
(63) Bitzek, E.; Koskinen, P.; Gähler, F.; Moseler, M.; Gumbsch, P. Structural Relaxation Made Simple. *Phys. Rev. Lett.* **2006**, *97*, No. 170201.
(64) Kelchner, C. L.; Plimpton, S.; Hamilton, J. Dislocation Nucleation and Defect Structure During Surface Indentation. *Phys. Rev. B* **1998**, *58*, 11085.
(65) Ruestes, C.; Bringa, E.; Gao, Y.; Urbassek, H. *Applied Nanoindentation in Advanced Materials*; Wiley-Blackwell, 2017; Chapter 14, pp 313−345.
(66) Larsen, P. M.; Schmidt, S.; Schiøtz, J. Robust Structural Identification via Polyhedral Template Matching. *Modell. Simul. Mater. Sci. Eng.* **2016**, *24*, No. 055007.
(67) Stukowski, A. Visualization and Analysis of Atomistic Simulation Data With OVITOThe Open Visualization Tool. *Modell. Simul. Mater. Sci. Eng.* **2010**, *18*, No. 015012.
(68) Stukowski, A. Structure Identification Methods for Atomistic Simulations of Crystalline. *Modell. Simul. Mater. Sci. Eng.* **2012**, *20*, No. 045021.
(69) Ziegenhain, G.; Urbassek, H. M.; Hartmaier, A. Influence of Crystal Anisotropy on Elastic Deformation and Onset of Plasticity in Nanoindentation: a Simulational Study. *J. Appl. Phys.* **2010**, *107*, No. 061807.
(70) Meyers, A.; Chawla, K. K. *Mechanical Behavior of Materials*; Cambridge University Press, 2009.
(71) Reissner, E. Stresses and Small Displacements of Shallow Spherical Shells. II. *J. Math. Phys.* **1946**, *25*, 279−300.
(72) Reissner, E.; Wan, F. Rotationally Symmetric Stress and Strain in Shells of Revolution. *Stud. Appl. Math.* **1969**, *48*, 1−17.
(73) Wan, F. Y.; Gregory, R. D.; Milac, T. I. A Thick Hollow Sphere Compressed by Equal and Opposite Concentrated Axial Loads: An Asymptotic Solution. *SIAM J. Appl. Math.* **1998**, *59*, 1080−1097.
(74) Chen, L. Y.; He, M.-r.; Shin, J.; Richter, G.; Gianola, D. S. Measuring Surface Dislocation Nucleation in Defect-Scarce Nanostructures. *Nat. Mater.* **2015**, *14*, 707−713.
(75) Brochard, S.; Hirel, P.; Pizzagalli, L.; Godet, J. Elastic Limit for Surface Step Dislocation Nucleation in Face-Centered Cubic Metals: Temperature and Step Height Dependence. *Acta Mater.* **2010**, *58*, 4182−4190.
(76) Bezares, J.; Jiao, S.; Liu, Y.; Bufford, D.; Lu, L.; Zhang, X.; Kulkarni, Y.; Asaro, R. J. Indentation of Nanotwinned fcc Metals: Implications for Nanotwin Stability. *Acta Mater.* **2012**, *60*, 4623−4635.
(77) Yin, J.; Retsch, M.; Thomas, E. L.; Boyce, M. C. Collective Mechanical Behavior of Multilayer Colloidal Arrays of Hollow Nanoparticles. *Langmuir* **2012**, *28*, 5580−5588.
(78) Ji, C.; Park, H. S. Characterizing the Elasticity of Hollow Metal Nanowires. *Nanotechnology* **2007**, *18*, No. 115707.
(79) Fioressi, S. E.; Bacelo, D. E.; Bozzolo, G.; Mosca, H. O.; del Grosso, M. F. Atomistic Modeling of Ag, Au, and Pt Nanoframes. *Comput. Mater. Sci.* **2015**, *98*, 142−148.
(80) Delogu, F. Atomistic Simulation of Decomposition Processes in Ag- Cu Hollow Nanocubes. *J. Phys. Chem. C* **2008**, *112*, 11135−11143.
(81) Enyashin, A. N.; Ivanovskii, A. L. Structural, Thermal Properties and Stability of Monolithic and Hollow MgO Nanocubes: Atomistic Simulation. *J. Mol. Struct.: THEOCHEM* **2007**, *822*, 28−32.
(82) Mueggenburg, K. E.; Lin, X.-M.; Goldsmith, R. H.; Jaeger, H. M. Elastic Membranes of Close-Packed Nanoparticle Arrays. *Nat. Mater.* **2007**, *6*, 656−660.

DOI: 10.1021/acs.jpcc.8b07242
J. Phys. Chem. C 2018, 122, 25035−25042